Computational exposition of multistable rhythms in 4-cell neural circuits

Krishna Pusuluri[1],

Neuroscience Institute, Georgia State University, Petit Science Center, 100 Piedmont Avenue, Atlanta, Georgia 30303, USA

Sunitha Basodi

Department of Computer Science, Georgia State University, 25 Park place NE, Atlanta, GA 30303, USA

Andrey Shilnikov

Neuroscience Institute, and Department of Mathematics and Statistics, Georgia State University, Petit Science Center, 100 Piedmont Avenue, Atlanta, Georgia 30303, USA

Abstract

Proper understanding of the co-existence of multistable rhythms generated by oscillatory neural circuits made up of 4 and more cells, their onset, stability conditions, and the transitions between such rhythms remains incomplete. This is partly due to the lack of appropriate visual and computational tools. In this study, we employ modern computational approaches including unsupervised machine learning (clustering) algorithms and fast parallel simulations powered by graphics processing units (GPUs) to further extend our previously developed techniques based on the theory of dynamical systems and bifurcations. This allows us to analyze the fundamental principles and mechanisms that ensure the robustness and multifunctionality of such neural circuits. In addition, we examine how network topology affects the dynamics, and the rhythmic patterns transition/bifurcate as network configurations are altered and the intrinsic properties of the cells and the synapses are varied. This study elaborates on a set of inhibitory coupled 4-cell circuits that can exhibit a variety of mono- and multistable rhythms including pacemakers, paired half-centers, traveling-waves, synchronized states, as well as various chimeras. Our detailed analysis is helpful to generate verifiable hypotheses for neurophysiological experiments with biological central pattern generators.

Keywords: Bifurcations, multistability, central pattern generators, unsupervised machine learning, dynamical systems, clustering, Poincaré return maps

1. Introduction

Rhythmic oscillations underlie a variety of sensory, motor and cognitive functions. Brain disorders such as schizophrenia, epilepsy, autism, Alzheimer's disease, and Parkinson's disease are characterized by dysfunction of neural oscillations. As such, mechanisms underlying rhythmic activities can help in designing therapeutic interventions for such conditions. Brain networks are composed of smaller structural and functional building blocks of neural networks called *motifs* [1, 2, 3, 4]. Such motifs have been identified in various animal central pattern generators (CPGs), which are biological neural networks producing rhythmic motor output without sensory feedback or central input. Rhythmic patterned motor activity under the control of CPGs is widespread across many vertebrate and invertebrate species in a diversity of neural networks including ones governing locomotion, swimming, respiration and heartbeat [5, 6, 7, 8, 9, 10, 11, 12, 4, 13, 14, 15, 16, 17]. As networks evolve and become more complex, the existing motifs are preserved while new elements are added to maximize the available number of configurations and to support the robustness of the networks [4, 18, 19, 20]. For example, a common constituent of many known CPGs is a half-center oscillator (HCO) that is made up of 2 bilaterally symmetric neurons that reciprocally inhibit each other to produce alternating bursting patterns in anti-phase. Multiple HCOs can be combined using chemical and/or electrical synapses to form complex modular CPG networks such as the well described swim CPGs in sea slugs *Melibe leonina* and *Dendronotus iris* [19, 21, 22, 11, 23, 24, 25, 26]. In order to gain insights into the dynamical principles that regulate the behaviors of larger networks, it is essential to understand the workings of individual neurons as well as the basic motifs. Mathematical modeling studies at multiple levels ranging from isolated neurons to small networks and populations have resulted in significant understanding of the working principles of biological neural networks [27, 28, 29, 30, 31, 32, 33].
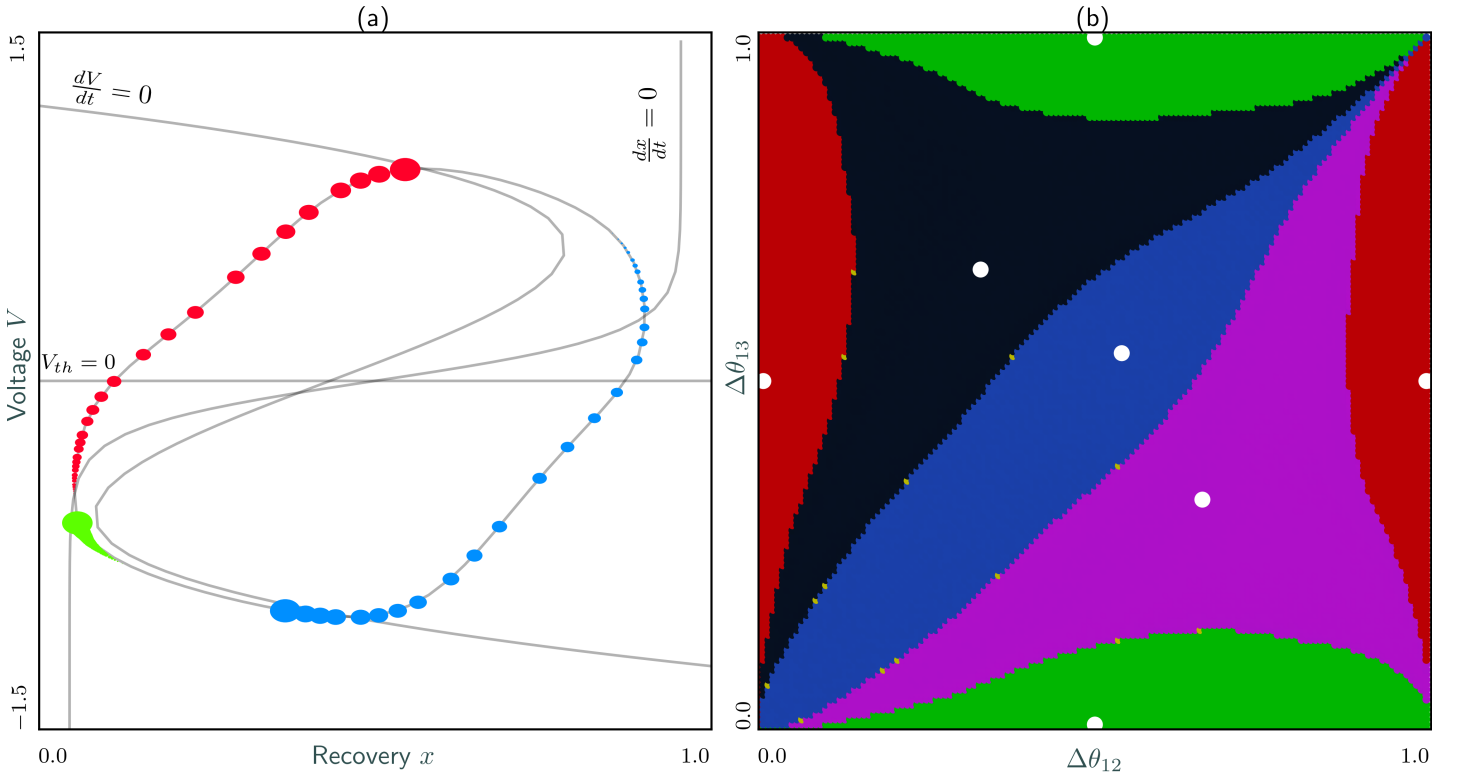
Figure 1: (a) The phase space of a weekly coupled *generalized* Fitzhugh-Nagumo type neuron with the slow recovery variable x and the fast voltage variable V, superimposed with the corresponding nullclines: slow $\frac{dx}{dt} = 0$ and fast $\frac{dV}{dt} = 0$, and the limit cycle. The colored dots depict the phase coordinates of three coupled cells traversing the limit cycle to generate a traveling-wave pattern (Fig.2c). (b) Multistability analysis of the fully connected 3-cell network (Fig. 2a) using the 2D Poincaré return map on a grid of 70×70 initial conditions or phase lags between cell 1 (blue - chosen as the reference cell) and cells 2 and 3. All the initial conditions that converge to the same attractor are shown in identical colors to visualize the attraction basins of the five co-existing fixed points (shown as white dots), representing five stable rhythms of the circuit. These are 3 pacemaker (red, green, and blue) and two travelling wave (pink - clockwise, black - anti-clockwise) rhythms. Fig. 2 shows sample trajectories converging to the blue pacemaker $(0.5, 0.5)$ and the clock-wise traveling-wave $(0.66, 0.34)$ (pink).

A fundamental challenge in theoretical and experimental research on CPGs is to understand the mechanisms by which such neural networks can adapt structurally and functionally to serve as dedicated circuits for monostable rhythms, or as multifunctional circuits producing several stable rhythmic behaviors [32, 20, 34, 35, 36, 37, 38, 39, 40]. Moreover, intrinsic capability for rhythm switching, such as gait transitions in locomotion and changes in the direction of blood flow in leeches, can be accomplished by input-driven perturbations that switch between multiple attractors representing various rhythmic patterns generated by a multistable CPG [18, 41, 42, 43]. In addition, these attractors, which can be fixed points or periodic orbits, can bifurcate – loose stability or vanish, thereby explaining the continuous or the sudden transitions in the system state due to changes in network connectivity, external inputs and the intrinsic dynamics of individual neurons [44]. The emergence of stable polyrhythms, and their transitions, exhibited by half-center oscillators and 3-cell motifs, along with their dynamics under the influence of external input and varying chemical (inhibitory and excitatory) and electrical synaptic connectivity, have been thoroughly demonstrated using Poincaré return maps for phase lags (described in the next section) and other techniques. Note that 4-cell circuits and more complicated CPGs that produce dedicated functionality have also been studied in real animals as well as computational models [18, 45, 46, 47, 48, 49, 34, 12, 4, 13, 14, 15, 16, 17]. The basic principles underlying the co-existence and stability of multiple rhythms in 4-cell networks and larger CPGs have long remained unclear, in part, due to the exponentially increasing algorithmic complexity and computational costs needed to systemically explore such networks. Another major problem with using the approaches like Poincaré return maps for larger networks is that, unlike the 3-cell circuits that are well described by 2-dimensional (2D) maps, the corresponding well populated maps for larger networks become 3D and higher dimensional, which are hard to analyze visually.

Traditional computational approaches using single threaded computing fall short both in terms of the amount of time required for the computations as well as the breadth and comprehensiveness that could be achieved. Recent advances in parallel processing and GPU computing with technologies such as CUDA, OpenAcc, OpenMP and OpenMPI offer tremendous performance improvements and make it possible to study problems in neuroscience and nonlinear dynamics that could not be solved earlier [50, 51, 52, 53, 54]. In this study, we will address the lack of such visual and computational tools and further extend the developed techniques based on dynamical systems theory for neuroscience applications by implementing elements of unsupervised machine learning for clustering analysis in higher dimensions [55, 56, 57, 58, 59, 60, 61] and GPU parallelization for faster simulations of densely populated trajectories in such coupled circuits. By combining the analytical tools with these computational approaches, we deconstruct the operating rules for the co-existence, stability and robustness of stable polyrhythms in complex CPGs. We demonstrate the effectiveness of this approach in homogenous 4-cell neural
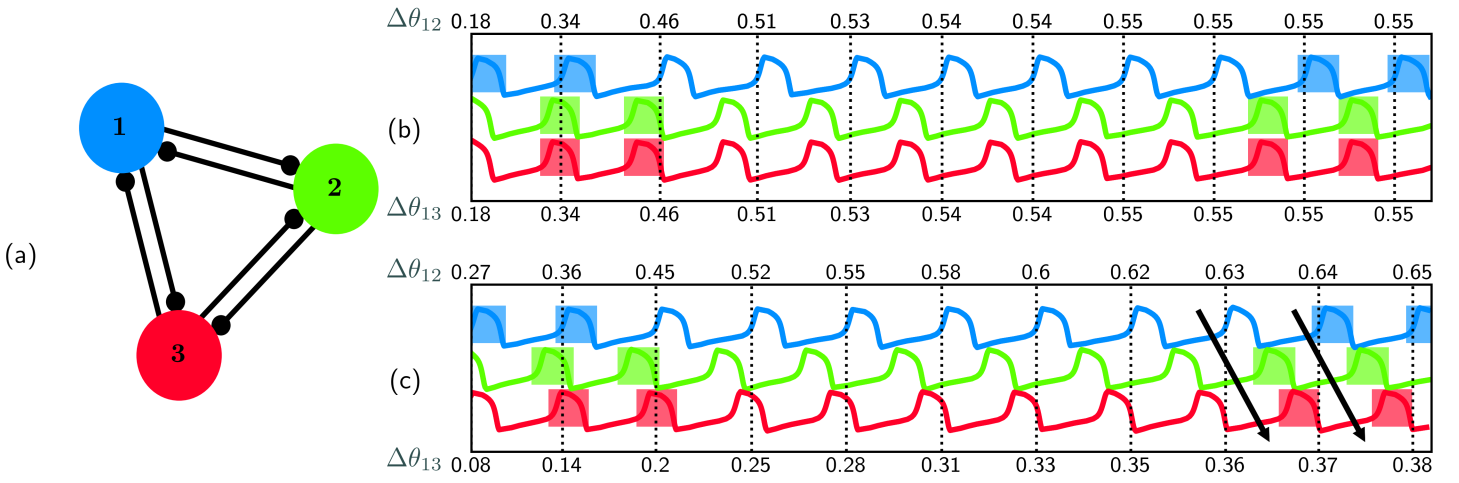
Figure 2: (a) A fully connected 3-cell network of the generalized Fitzhugh-Nagumo type cells with mutually inhibitory synapses. Two long trajectories converging towards (b) the blue pacemaker rhythm ($\Delta\theta_{12}$, $\Delta\theta_{13}$) = (0.55, 0.55) or (c) the clockwise traveling-wave rhythm ($\Delta\theta_{12}$, $\Delta\theta_{13}$) = (0.67, 0.33) are shown. Evolution of the phase lags $\Delta\theta_{12}$ and $\Delta\theta_{13}$ at those moments when the reference cell 1 (blue) crosses above threshold (vertical dotted lines) are shown at the top and the bottom, respectively. Here, $I_{app} = 0.426$, $g_{inh} = 0.01$ and $\varepsilon = 0.3$.

circuits with inhibitory coupling and show how network topologies, intrinsic and extrinsic parameters result in bifurcations and alter network behaviors. The development and incorporation of such mathematical and computational tools is essential to unravel the multifarious behaviors arising in neuroscience. The methods developed are interdisciplinary with applications to complex dynamical systems and networks of coupled oscillators ranging across (electro)chemical reactions, population dynamics, electronic circuits, nonlinear optics, regulatory genetic networks and excitatory dynamics of cellular membranes and heart beats, to name a few.

2. Models and numerical methods

We construct our neural circuits using identical neurons of a *generalized* Fitzhugh-Nagumo type with a cubic fast nullcline and a sigmoidal slow nullcline as described in [43]. The equations are given by:

$$
\begin{aligned}
\frac{dV_i}{dt} &= V_i - V_i{}^3 - x_i + I_{app} + \sum_{j \neq i} g_{inh}^{ji}\, G(V_i, V_j) \\
\frac{dx_i}{dt} &= \varepsilon\, [x_\infty(V_i) - x_i]
\end{aligned}
\tag{1}
$$

The voltage variable V_i and the recovery variable x_i together determine the state of the ith neuron. The parameter ε for time-scale separation determines the slow dynamics of x_i with respect to V_i; the slow nullcline $\frac{dx_i}{dt} = 0$ is given by the sigmoidal function:

$$
x_\infty(V_i) = \frac{1}{1 + e^{-10\,(V_i - V_{sh})}} \quad \text{where} \quad V_{sh} = 0.
$$

Parameter values are initially chosen so that the system has a unique repelling equilibrium state at the intersection of the middle, unstable branch of the V-nullcline (where $\frac{dV}{dt} = 0$) and the slow x-nullcline (where $\frac{dx}{dt} = 0$), surrounded by a stable limit cycle, as shown in Fig. 1a. The reciprocal interactions between these two variables result in oscillatory behavior through dynamical hysteresis where the voltage variable becomes bistable between the active ($V_i \geq V_{th}$) and the inactive ($V_i < V_{th}$) states for a fixed value of the recovery variable, with the activation threshold given by $V_{th} = 0$. Relaxation oscillations are constituted by the relatively slow transient active and inactive meta-states and the fast switching between the corresponding branches (for $0 < \varepsilon < 1$). The external drive I_{app} horizontally shifts the position of the V-nullcline and controls the release and escape mechanisms of the otherwise stationary states of the neuron [43].

Inhibitory synaptic coupling between the neurons in a network is modeled using fast-threshold modulation with a sigmoidal coupling function. An inhibitory synapse, due to $E_{rev} = -1.5$, from neuron j to neuron i, with strength g_{inh}^{ji} in equation (1) is given by

$$
G(V_i, V_j) = (E_{rev} - V_i)\, \Gamma(V_j), \quad \text{where} \quad \Gamma(V_j) = \frac{1}{1 + e^{-100\,(V_j - E_{th})}}, \text{ and } E_{th} = 0
$$

The voltage variable V_i is driven by a summation of such synaptic inputs from all other neurons $j \neq i$ in the circuit. Identical values are used for all the synaptic strengths g_{ji} within a network, except where specified otherwise. The external drive I_{app}, the time-scale constant ε, and the network coupling strength g_{inh} serve as key bifurcation parameters that determine the circuit dynamics. The choice of the model used in the study provides computational simplicity while retaining
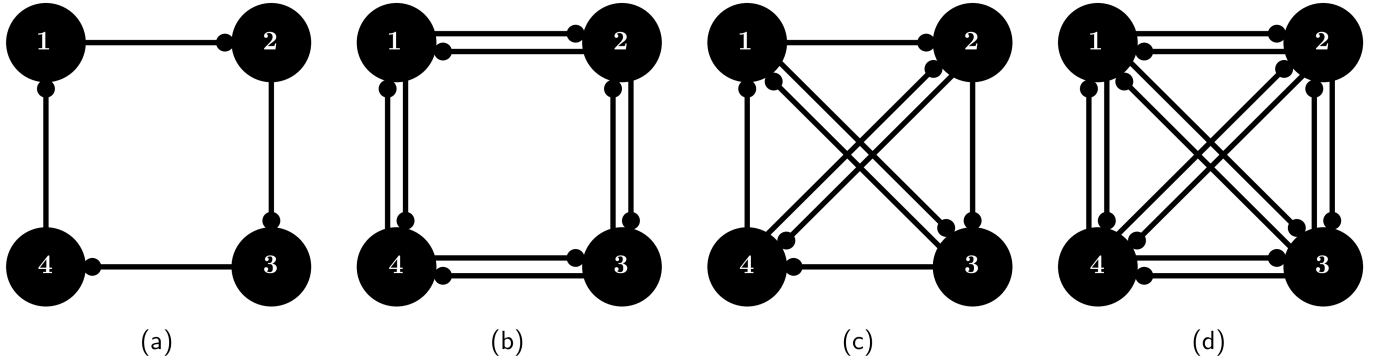
3

Figure 3: Homogenous network topologies for 4-cell circuits with inhibitory synaptic coupling between neurons: (a) One-way inhibitory loop (b) Two-way inhibitory loop (c) Mixed (d) Fully connected. In each of these network configurations, all the neurons have identical parameter values and receive the same number of incoming synapses of identical strengths.

the essential dynamical features and mechanisms of rhythmogenesis seen in the detailed Hodgkin-Huxley type of neuronal models. Further details of this neuron model and the multistability analysis of 3-cell networks can be found in [43], while such analysis for detailed Hodgkin-Huxley type of neurons is presented in [18].

2.1. Poincaré return maps for phase lags

Figure 2a shows a 3-cell motif comprised of generalized Fitzhugh-Nagumo type neurons with mutually inhibitory synapses, as described by equations (1). Figures 2b,c show two voltage traces that converge to stable pacemaker (blue) and traveling-wave (clockwise) rhythms with phase-locked states in this network. The possible polyrhythms in such 3-cell motifs have been previously described using Poincaré return maps for phase lags (see Fig. 1b) to determine the attraction basins, stability and bifurcations of the fixed points corresponding to phase locked states in the voltage patterns [18, 43, 62, 63, 37, 38]. These maps are built using specific events in time when the cells cross the threshold voltage from below. A sequence of phase lags is defined for each cell, as the delay in the burst initiation of a reference cell with respect to that of this cell, normalized over the bursting period. Thus, in the 3-cell CPG shown in Fig. 2a, if t_1^n, t_2^n, and t_3^n represent the times at which cell 1 (blue), cell 2 (green) and cell 3 (red) cross the threshold for the nth time, using cell 1 as the reference cell, the (n^{th}) phase lags are given by:

$$\Delta\theta_{12} = \frac{t_1^{n+1} - t_2^n}{t_2^{n+1} - t_2^n} \ \text{ and } \ \Delta\theta_{13} = \frac{t_1^{n+1} - t_3^n}{t_3^{n+1} - t_3^n}$$

Ordered pairs of phase lags ($\Delta\theta_{12}$, $\Delta\theta_{13}$) are used to construct a Poincaré return map in the 2D discrete phase space. A sequence of ordered pairs yields a forward phase trajectory on a 2D torus (Fig. 1b), which maps the phases of cells 2 and 3 with respect to the reference cell 1, defined for values between 0 and 1. A phase lag of either 0 or 1 represents an in-phase relationship with the reference cell while a phase lag of 0.5 represents an anti-phase relationship. A fixed point in the system corresponds to a stable rhythmic oscillatory pattern that arises out of well defined phase lags between the burst initiations of individual neurons of the CPG, which remain phase-locked over time. All trajectories starting from a wide range of initial phase lags that converge to the same fixed point or stable rhythm are marked by identical colors, depicting the attractor of the rhythm in the phase space. By analyzing the phase space of the Poincaré map, it is possible to predict the characteristics of the rhythmic behaviors of the corresponding CPG. The Poincaré map in Fig. 1b reveals the existence of a penta-rhythmic state in the CPG with 3 pacemakers (blue - Fig. 2b, green and red) and two traveling-waves (pink - Fig. 2c, black). The blue, green and red pacemakers correspond to the fixed points on the Poincaré map represented by the ordered pairs $(0.5, 0.5)$, $(0.5, 0)$ and $(0, 0.5)$ respectively, for the phase lags ($\Delta\theta_{12}$, $\Delta\theta_{13}$), while the clockwise (pink) and anti-clockwise (black) traveling-waves are represented by $(0.67, 0.33)$ and $(0.33, 0.67)$, respectively. Using Poincaré return maps for phase lags, the problem of existence and stability of multiple bursting rhythms in the CPG is reduced to the bifurcation analysis of fixed points, attractors and invariant cycles in the system.

2.2. Unsupervised machine learning

In order to analyze multistability of larger networks whose corresponding Poincaré return maps are of dimension 3D and higher, we employ unsupervised machine learning techniques to computationally evaluate the attraction basins of the stable polyrhythms (read stable fixed points), and analyze their corresponding bifurcations. We investigate multi-stable dynamics in homogenous networks comprised of 4 generalized Fitzhugh-Nagumo type neurons given by equations (1), with identical mutual inhibition between neurons. Such a model provides computational simplicity while showing the dynamics
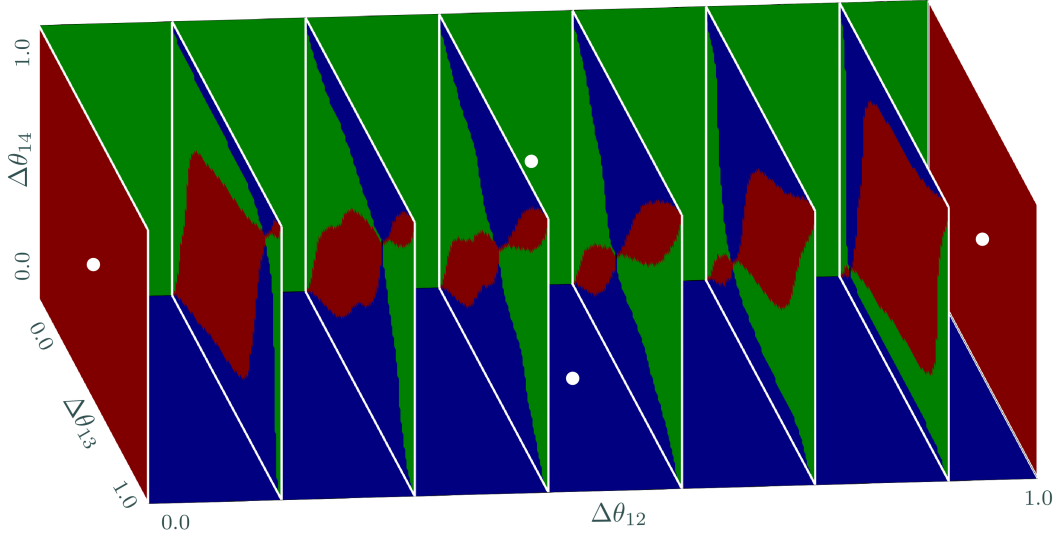
Figure 4: A sliced 3D torus of the Poincaré return map for phase lags for the fully connected 4-cell circuit (Fig. 3d) shows the inner structure of the attraction basins. Green, blue and red attractor basins of the corresponding fixed points (white dots) represent the stable paired half-center rhythms whose phase lag ordered tuples ($\Delta\theta_{12}$, $\Delta\theta_{13}$, $\Delta\theta_{14}$) are given by $(0.5, 0., 0.5)$, $(0.5, 0.5, 0.)$, and $(0., 0.5, 0.5)$, respectively. Here $g_{inh} = 0.025$, $I_{app} = 0.575$ and $\varepsilon = 0.5$.

topologically similar to more complex models based on the Hodgkin-Huxley formalism [43, 18]. For meaningful application of Poincaré maps, homogeneity ensures similar bursting periods across different neurons by (1) using identical parameter values for all the neurons and (2) keeping the sum of the synaptic strengths of all the inputs received by a neuron the same as those of any other neuron in the network. Figure 3 shows various homogenous network topologies for the 4-cell circuits, with gradually increasing complexity, starting from the one-way inhibitory loop (Fig. 3a), to the two-way inhibitory loop (Fig. 3b), to the mixed network (Fig. 3c), and finally the fully connected network (Fig. 3d).

We analyze the Poincaré return maps using hierarchical clustering schemes [55, 56, 57, 58, 59, 60, 61]. We begin by first identifying multiple initial conditions with varying phase lags for the cells, spread out uniformly across the 3D phase torus on a $(25 \times 25 \times 25)$ grid. For each of those initial conditions, we obtain long traces of firing activity of the circuit and compute the corresponding phase trajectory of ordered tuples ($\Delta\theta_{12}$, $\Delta\theta_{13}$, $\Delta\theta_{14}$) of phase lags. Using clustering methods, all the trajectories from different initial conditions that converge to a very close neighborhood of each other are determined to be within a cluster. Since the phase lags are defined on the 3D torus with modulo-1, implying the phase lags 0.0 and 1.0 are identical, the circular mean of all the converging ordered tuples of phase lags of the trajectories within a cluster defines the fixed point or the stable rhythm marked by the cluster. We also measure the circular standard deviation to reflect the degree of variability within a cluster. Circular means and circular standard deviations are rounded up to two decimal points. The total number of initial conditions whose trajectories converge to each cluster serves as a measure for the relative size of the attraction basin of the stable rhythm. Numerical integration is performed using the fourth order Runge-Kutta method with a fixed step size. Computation of neural trajectories and phase lags, and parallelization across GPU threads is achieved using CUDA and OpenAcc [6]. Clustering analysis and visualizations are done using Python.

For example, Fig. 4 represents a Poincaré return map on the 3D phase torus using multiple 2D slices for the fully connected 4-cell circuit (see Fig. 3d). It shows three distinct attractors (with green, blue, and red basins) of the paired half-center rhythms, where two pairs of cells fire in anti-phase while cells within a pair fire in synchrony (see Fig. 6 paired half-center). The phase lag ordered tuples ($\Delta\theta_{12}$, $\Delta\theta_{13}$, $\Delta\theta_{14}$) for these rhythms are given by $(0.5, 0., 0.5)$, $(0.5, 0.5, 0.)$, and $(0., 0.5, 0.5)$ for the green, blue, and red attractors, respectively. Constructing and decoding such 3D phase space trajectories visually is rather hard and time consuming. Table 1 illustrates the results of the clustering approach to automate the detection of these multistable states (fixed points), the phase relationships of the cells at these attractors, the degree of variability in their convergence, and the relative sizes of the attraction basins of various rhythmic states by means of cluster

Table 1: Multistability analysis of the fully connected 4-cell CPG (Fig. 3d) with 3D phase torus of Poincaré maps (Fig. 4) is simplified using clustering to reveal three stable paired half-center rhythms.

CCM	CCSD	PC
(0.5, 0., 0.5)	(0., 0., 0.)	33.2%
(0.5, 0.5, 0.)	(0., 0., 0.)	33.5%
(0., 0.5 ,0.5)	(0., 0., 0.)	33.2%

$g_{inh} = 0.025$, $I_{app} = 0.575$ and $\varepsilon = 0.5$

circular means (CCM), cluster circular standard deviations (CCSD) and the percentage of convergence (PC). We stress that GPU parallelization allows this multistability analysis to be performed within just a couple of minutes.
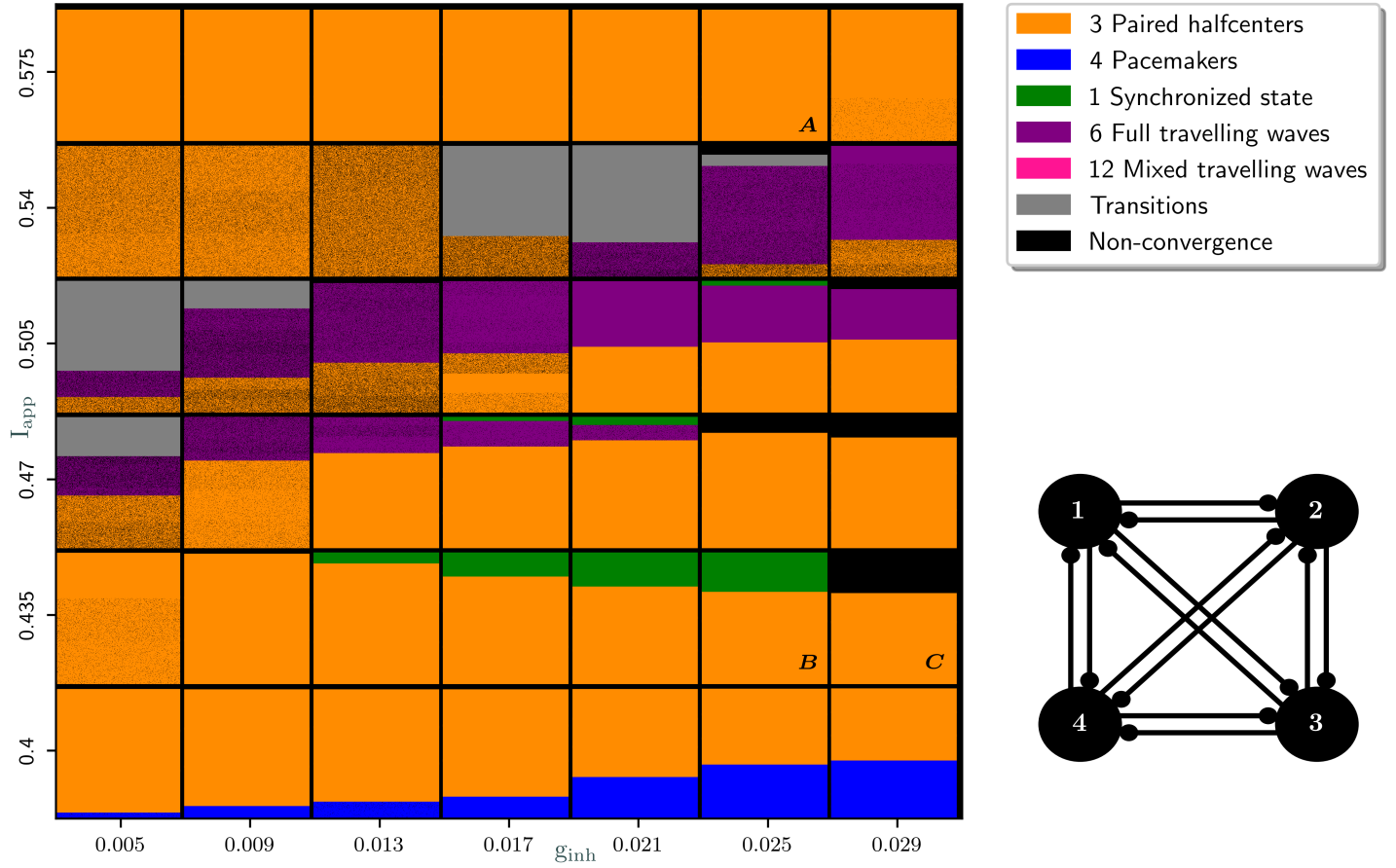
Figure 5: Multistability and bifurcation analysis of the fully connected 4-cell circuit with varying synaptic strength (g_{inh}) and external drive (I_{app}) on a 7×6 grid, at $\varepsilon = 0.5$. Each block in the grid depicts the clusters and the stable rhythms identified for the particular parameter values, shown in different colors in proportion to the size of their attraction basins in the phase space. Noise within a cluster is proportional to its circular standard deviation. 3D phase torus and clustering results for some of these parametric blocks are shown in Fig. 4 and Table 1,2. The bifurcation diagram identifies the rich repertoire of stable rhythms and all their isomorphisms expected from the symmetry of the circuit, including paired half-centers, pacemakers, traveling-waves, synchronization, stable transitory rhythms, and trajectories with non-converging phase lags (chimeras), as pictured in Fig. 6.

3. Results

We investigate the multistable rhythms generated by various homogenous network configurations of 4-cell CPGs given in Fig. 3. We find the network topologies that drive monostable or multistable behaviors. We also identify the transitions occurring in these networks as parameters such as the synaptic and external drives are varied, to determine the principles underlying stable polyrhythms in such networks.

3.1. Multifunctionality repertoire of the fully connected network

Figure 5 is an illustration of the multistability and bifurcation analysis performed on the fully connected 4-cell circuit, as we vary two parameters of the network, the synaptic strength (g_{inh}) and the external drive (I_{app}), on a 7×6 grid, while keeping a fixed $\varepsilon = 0.5$. For each set of parameters in this grid, the clustering analysis of Poincaré return maps of the 3D torus is performed to identify the stable rhythmic behaviors (clusters). Each block in the grid represents the clusters and the rhythmic behaviors identified for the particular parameter values. The rhythmic state associated by each cluster is given by the cluster circular mean (CCM). The homogeneity and symmetry of the network implies that circular permutations or symmetric variations or isomorphisms of the rhythms coexist in the network. For example, the orange block marked A at $g_{inh} = 0.025$ and $I_{app} = 0.575$ represents the existence of 3 stable isomorphisms of the paired half-center rhythms whose phase lag ordered tuples ($\Delta\theta_{12}$, $\Delta\theta_{13}$, $\Delta\theta_{14}$) are given by $(0.5, 0., 0.5)$, $(0.5, 0.5, 0.)$, and $(0., 0.5, 0.5)$. Cell 1 could fire in phase with either of cells 2, 3 or 4, while the remaining two cells fire in anti-phase relationship with cell 1 (and synchronously with each other). This is also shown in the clustering results and the 3D phase torus of Fig. 4 and Table 1. For any given parametric block of Fig. 5, each color indicates the existence of a stable rhythm, along with all of its isomorphisms. Multiple colors within the same block indicate the co-existence of different stable rhythmic patterns in the phase space. The sizes of the colored regions proportionally relate to the sizes of the attraction basins of those rhythms, given by the percentage of trajectories converging to those rhythms (PC). Noise within the colored region representing a cluster is proportional to
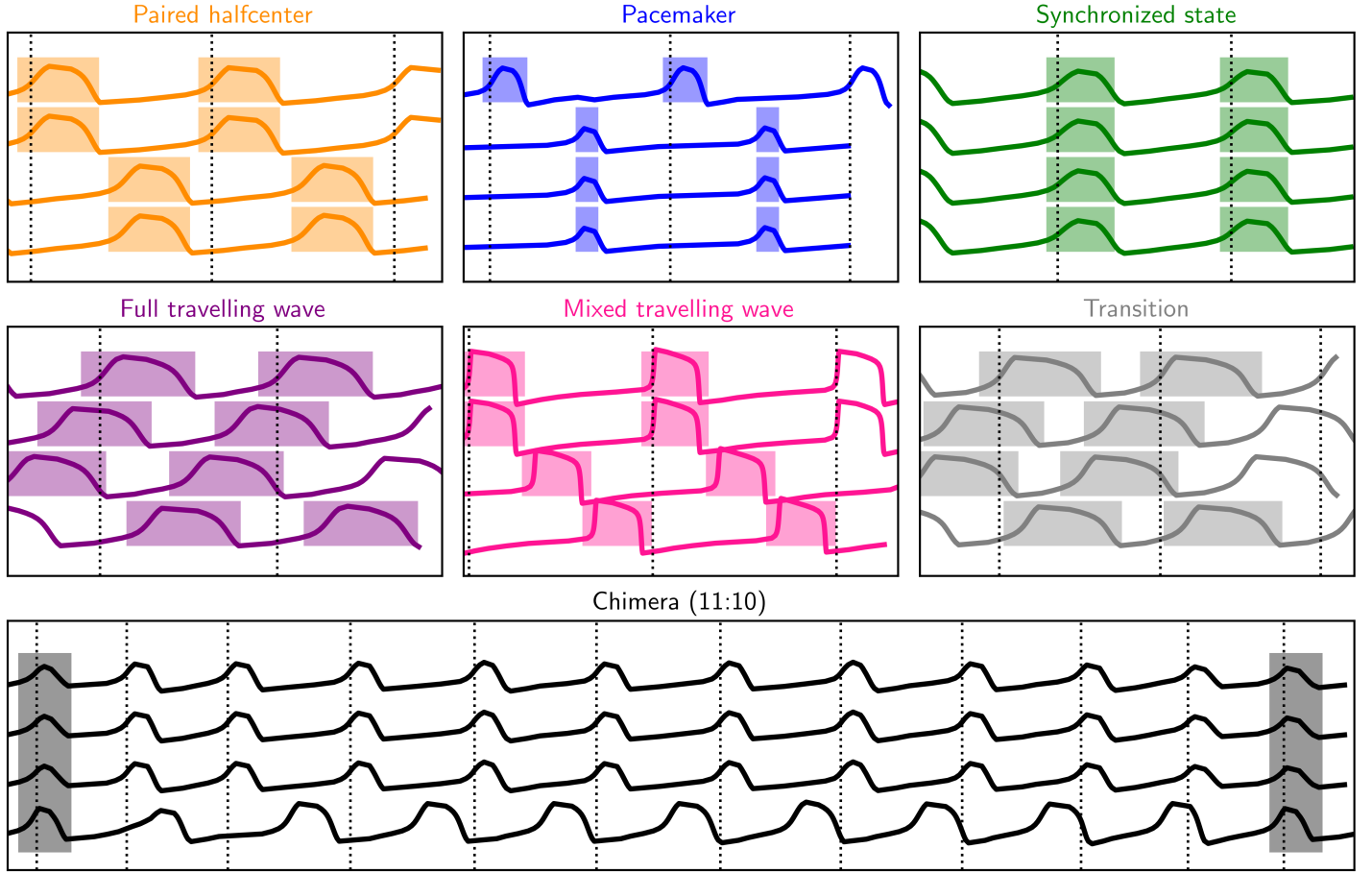
6

Figure 6: Rhythmic capacity of the fully connected 4-cell circuit (Fig. 3d), depending on the parameter values (see Fig. 5), includes 3 paired half-centers, 4 pacemakers, a single fully synchronous state, 6 full traveling-waves, 12 mixed traveling-waves, stable transitory rhythms between paired half-centers and full traveling-waves, and 4 chimera states featuring a 11:10 resonance.

the cluster's circular standard deviation (CCSD) and is indicative of the variability within the cluster. The clustering analysis for the network across different g_{inh} vs. I_{app} blocks at $\varepsilon = 0.5$ in Fig. 5 shows that the network can exhibit a plethora of different stable rhythms, pictured in Fig. 6. Clustering details with CCM, CCSD and PC at some of these parametric blocks are presented in Table. 2. Mixed traveling-waves are seen at a different $\varepsilon = 0.05$ (see supplementary Fig.S2).

3.1.1. Paired half-centers

This is the most dominant rhythm of the fully connected network as seen from the bifurcation diagram of Fig. 5 (orange regions such as A) at $\varepsilon = 0.5$, as well as at $\epsilon = 0.3$ shown in the bifurcation diagram of supplementary Fig. S1. These 2-phasic rhythms are characterized by two pairs of cells that oscillate in anti-phase relationship with each other, while the cells within each pair oscillate in-phase (supplementary Movie. M2). By virtue of symmetry of the fully connected network, there exist 3 stable isomorphisms of this rhythm. The phase-lag ordered tuple for one such rhythm is given by ($\Delta\theta_{12}$, $\Delta\theta_{13}, \Delta\theta_{14}) = (0., 0.5, 0.5)$ and is shown in Fig. 6, while the corresponding limit cycle orbit of the voltage and the recovery variables is represented in Fig. 7 (orange). Note here that the voltage amplitude of the orbit for the paired half-center rhythm is slightly smaller than that of an isolated cell (grey), due to the continuous inhibition experienced by a cell in its active state from its phase locked counterpart.

3.1.2. Synchronized state

Surprisingly, we see that the fully connected network of neurons reciprocally coupled with fast-inhibition can also exhibit stable synchronization of neuronal activity with ($\Delta\theta_{12}$, $\Delta\theta_{13}$, $\Delta\theta_{14}) = (0., 0., 0.)$, for particular values of the parameters: $I_{app} = 0.435$ and for $0.013 \leq g_{inh} \leq 0.025$ (see green regions in Fig. 5, and supplementary Movie. M3). The synchronized state coexists with the 3 paired half-center rhythms at these parameter values. The corresponding orbit for the voltage and recovery variables is shown in Fig.7 (green). The voltage amplitude of this orbit is even shorter than those of either the isolated cell (grey) or the paired half-center rhythm (orange), due to the greater inhibitory push experienced by a neuron in its active state from the 3 other phase locked counterparts. With increasing g_{inh} in Fig. 5, the size of the attractor for the

synchronized state gradually increases through $g_{inh} = 0.025$ (Fig. 5B), beyond which it loses stability and gives rise to a chimera state at $g_{inh} = 0.029$ (Fig. 5C). Note that the stable synchronized state is seen in the network only at $\varepsilon = 0.5$ (Fig. 5) but not at either $\varepsilon = 0.3$ (supplementary Fig. S1) or $\varepsilon = 0.05$ (supplementary Fig. S2). We also note that, as $I_{app} = 0.435$ and $g_{inh} = 0.025$ are kept constant (see Fig. 5B) while ε is gradually reduced from 0.5 to 0.48, the corresponding synchronized orbit undergoes period doubling such that all the four cells yet continue to maintain phase synchrony, while splitting into two pairs that continuously alternate between orbits of slightly shorter and longer amplitudes (as depicted in supplementary Movie. M4).

3.1.3. Chimera states

Further increase of g_{inh} through 0.029 at $I_{app} = 0.435$ (see Fig. 5C) shows a non-converging state (black regions) from the clustering analysis of Poincaré maps. Detailed inspection reveals the presence of chimera states characterized by two sub-populations firing at distinct frequencies. Three of the cells continuously fire in phase, while the fourth cell experiences phase slipping and synchronizes with the other three once every 10 cycles, when those cells complete 11 cycles, thereby resulting in a chimera with a 11:10 resonance as shown in Fig. 6. Note the shorter voltage amplitude of the three cells firing in sync compared to the cell undergoing phase slipping, for reasons described previously. By virtue of the symmetry of the network, there exist four isomorphisms of this rhythm, with any one of the four cells undergoing phase slipping while the other three fire in phase. Further increase of g_{inh} to 0.033 (not shown in Fig. 5) results in the chimera states morphing into pacemaker rhythms. Thus, the chimera state serves as a transition mechanism between the synchronized state and the pacemaker patterns. At other values of the parameters, we also observe chimera states with different resonances, including 7:8 resonance at $\varepsilon = 0.55$ and 14:16 resonance at $\varepsilon = 0.56$ for $g_{inh} = 0.025$ and $I_{app} = 0.435$.

Figure 7: Voltage-recovery phase space shows how the limit cycle of an isolated neuron (grey) changes its shape in a fully connected 4-cell circuit based on its initial conditions, to produce either a paired half-center rhythm (orange) or the synchronized state (green) (Fig. 5B). The size of the orbit for the paired half-center (orange) is smaller than that of an isolated cell (grey) due to the continuous inhibition from their phase locked counterparts affecting the cells in their active state (and shortening the corresponding section of the limit cycle). For the synchronized state, the orbit becomes even smaller (green) due to the greater consolidated inhibition on a postsynaptic cell by the 3 other cells in sync.

3.1.4. Pacemakers

At small values of external drive $I_{app} = 0.4$, the fully connected network can exhibit 2-phasic pacemaker rhythms co-existing with the paired half-center rhythms (Fig. 5, supplementary Fig. S1). These rhythms are characterized by one cell driving the rhythm and firing in antiphase with three other cells that oscillate in-phase. Four stable isomorphisms exist for this rhythm, with each of the four cells capable of driving such a pacemaker pattern. The phase lag ordered tuple for one such rhythm is given by $(\Delta\theta_{12}, \Delta\theta_{13}, \Delta\theta_{14}) = (0.5, 0.5, 0.5)$ and is shown in Fig. 6, which also reveals the shorter voltage amplitudes of the three driven cells in comparison to that of the driving pacemaker cell.

3.1.5. Traveling-waves

The network can produce 6 isomorphisms of a full 4-phasic traveling-wave rhythm, where the cells fire sequentially one after the other in a cyclic fashion (see Fig. 5, supplementary Fig. S1, supplementary Fig. S2, and supplementary Movie. M1). The phase-lag ordered tuple for one such rhythm is given by $(\Delta\theta_{12}, \Delta\theta_{13}, \Delta\theta_{14}) = (0.25, 05., 0.75)$, while the corresponding voltage trace is depicted in Fig. 6. We observe that at $\varepsilon = 0.05$ (Supp.Fig. S2), the network can also exhibit a different type of traveling-wave rhythm that is referred to as a *mixed* 3-phasic traveling-wave, where two cells fire in phase while oscillating sequentially with the other two cells. The network can produce a total of 12 isomorphisms of such mixed traveling-wave rhythms; one is shown in Fig. 6 with the phase lags locked at $(\Delta\theta_{12}, \Delta\theta_{13}, \Delta\theta_{14}) = (0., 0.67, 0.33)$.
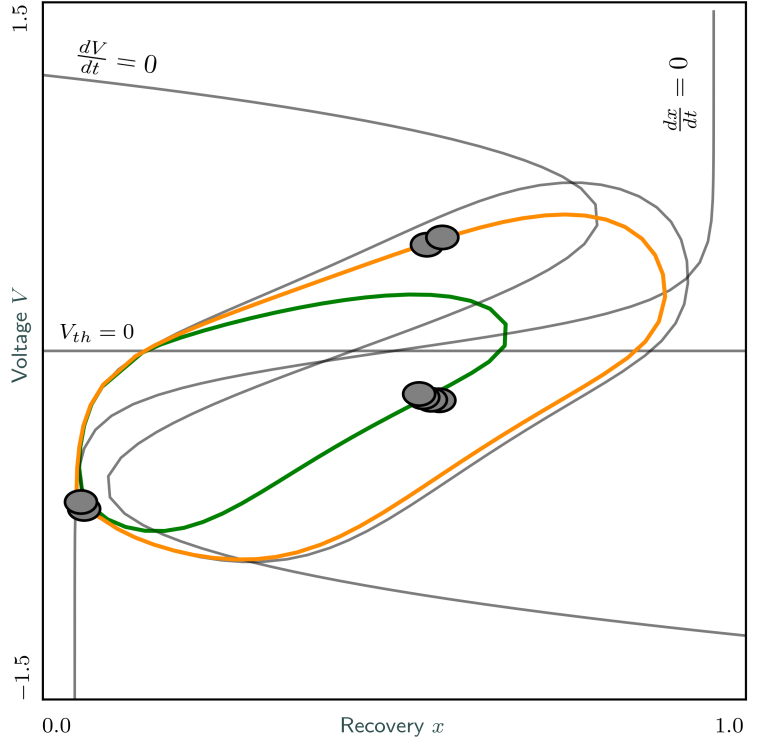
3.1.6. Stable transitions

Figure 6 shows a stable "transitory" rhythm given by $(\Delta\theta_{12}, \Delta\theta_{13}, \Delta\theta_{14}) = (0.41, 0.5, 0.91)$ at $g_{inh} = 0.025$ and $I_{app} = 0.552$. Such rhythms serve as stable intermediate states between some of the rhythms previously described. As we move downward from Fig. 5A where there are just 3 paired half-center rhythms at $I_{app} = 0.575$, the system gives rise to 6 full traveling-wave rhythms at $I_{app} = 0.505$, in addition to the 3 paired half-centers. Between these values of I_{app}, the full traveling-waves lose stability via a supercritical pitch fork bifurcation and give rise to two such stable transitory rhythms (grey). For example, when the full traveling-wave given by $(\Delta\theta_{12}, \Delta\theta_{13}, \Delta\theta_{14}) = (0.25, 0.5, 0.75)$ loses stability, the anti-phase relationships $\Delta\theta_{13} = 0.5$ and $\Delta\theta_{24} = 0.5$ are maintained, but the active phase of cell 1 could get closer and closer to that of either of cell 2 or 4, while the phases of the remaining two cells also start getting closer and closer, until they give rise to either of the paired half-centers given by $(0., 0.5, 0.5)$ (1,2 vs. 3,4) or $(0.5, 0.5, 0.)$ (1,4 vs. 2,3). Therefore, for intermediate values of I_{app}, we could gradually see stable transitory rhythm pairs such as $(0.15, 0.5, 0.65)$, $(0.35, 0.5, 0.85)$, and $(0.05, 0.5, 0.55)$, $(0.45, 0.5, 0.95)$.

3.2. Robust monostable/bistable network topologies

Multistability and bifurcation analysis for the other 4-cell network topologies of Fig. 3 (see supplementary Fig.S3,S4,S5) shows that the two-way inhibitory loop (Fig. 3b) and mixed (Fig. 3c) networks exhibit robustly monostable rhythms (their g_{inh} vs. I_{app} parametric sweeps show a single stable rhythm across all parametric blocks) given by the phase lag ordered tuples $(0.5, 0., 0.5)$ (paired half-center) and $(0.25, 0.5, 0.75)$ (full traveling-wave), respectively, while the one-way inhibitory loop network (Fig. 3a) exhibits robust bistability with both these rhythms $(0.5, 0., 0.5)$ and $(0.25, 0.5, 0.75)$, as the parameters g_{inh}, I_{app}, and ε are varied. Note that no other stable isomorphisms of these full traveling-wave and paired half-center rhythms are stable in these network configurations due to the missing connections from the fully connected circuit (Fig. 3a). Compare the full traveling-wave rhythm of the mixed network (Fig. 3c) with a similar reduced swim CPG found in the sea slug *Melibe leonina* (with additional excitatory connections) [39, 25] (see Fig. 3.3 from Ref. [39]). Neurophysiological experiments with this CPG reported the occurrence of a similar full traveling-wave pattern in the voltage traces.

3.3. Network transitions/rewiring

Our approach can generate verifiable hypotheses for experimental manipulations and rewiring of real animal CPGs with dynamic clamping experiments [64]. We can investigate how network topologies and synaptic changes can alter the rhythmic behavior of the network and promote or suppress multistability. Fig. 8 shows the functional changes in CPG rhythms and their mono/multi-stable behaviors due to structural changes in network topology. The network on the left is gradually transitioned into the network on the right by synaptic changes, while the rhythmic behaviors and multistability are analysed during these transitions. Purple regions represent the full traveling-wave rhythm $(0.25, 0.5, 0.75)$ while orange regions represent the paired half-center $(0.5, 0., 0.5)$, with sizes proportional to their attractors in the phase space. Gradual strengthening of the anti-clockwise inhibitory connections in Fig. 8a converts the bistable one-way inhibitory loop network into the monostable two-way inhibitory loop network. The paired half-center rhythm is promoted while the traveling-wave rhythm is suppressed. In Fig. 8b, mutual inhibitions between cells 1,3 and cells 2,4 are gradually strengthened to convert the bistable one-way inhibitory loop network on the left to the monostable mixed network on the right. The traveling-wave rhythm is gradually promoted while the paired half-center rhythm is suppressed. In Fig. 8c, by gradually weakening the anti-clockwise inhibitory loop and simultaneously strengthening mutual inhibitions between cells 1,3 and cells 2,4, the network transitions from one monostable rhythm (paired half-center) to another (full traveling-wave). At intermediate synaptic changes, the network is bistable. Also, note that at such intermediate stages, the synaptic strengths in the network are not all identical, but the homogeneity of the neurons in the network is maintained, with all of them receiving similar total synaptic inputs.

Table 2: Details of the clustering analysis for multistability of the fully connected network at three representative parametric blocks of Fig. 5 at $g_{inh} = 0.025$ and $\varepsilon = 0.5$.

| I_{app}	CCM	CCSD	PC
0.4	(0.5, 0., 0.5)	(0., 0., 0.)	18.9%
	(0.5, 0., 0.)	(0., 0., 0.)	8.9%
	(0.5, 0.5, 0.5)	(0., 0., 0.)	15.8%
	(0.5, 0.5, 0.)	(0., 0., 0.)	18.8%
	(0., 0., 0.5)	(0., 0., 0.)	8.9%
	(0., 0.5, 0.5)	(0., 0., 0.)	18.9%
	(0., 0.5, 0.)	(0., 0., 0.)	9.3%
0.435	(0., 0., 0.)	(0., 0., 0.)	28.5%
	(0., 0.5, 0.5)	(0., 0., 0.)	23.9%
	(0.5, 0., 0.5)	(0., 0., 0.)	23.8%
	(0.5, 0.5, 0.)	(0., 0., 0.)	23.8%
0.54	(0.5, 0.25, 0.74)	(-0., 0.02, 0.02)	12.7%
	(0.74, 0.25, 0.5)	(0.03, 0.03, -0.)	12.6%
	(0.25, 0.5, 0.74)	(0.03, -0., 0.03)	12.4%
	(0.25, 0.74, 0.5)	(0.03, 0.03, -0.)	12.9%
	(0.74, 0.5, 0.25)	(0.02, -0., 0.02)	12.8%
	(0.5, 0.74, 0.25)	(-0., 0.03, 0.03)	12.7%
	(0.49, 0.98, 0.49)	(0.03, 0.04, 0.04)	4.3%
	(0.95, 0.47, 0.48)	(0.03, 0.03, 0.03)	2.6%
	(0.05, 0.52, 0.53)	(0.03, 0.03, 0.04)	3.1%
	(0.48, 0.47, 0.95)	(0.03, 0.04, 0.03)	1.5%
	(0.53, 0.53, 0.05)	(0.04, 0.04, 0.04)	6%
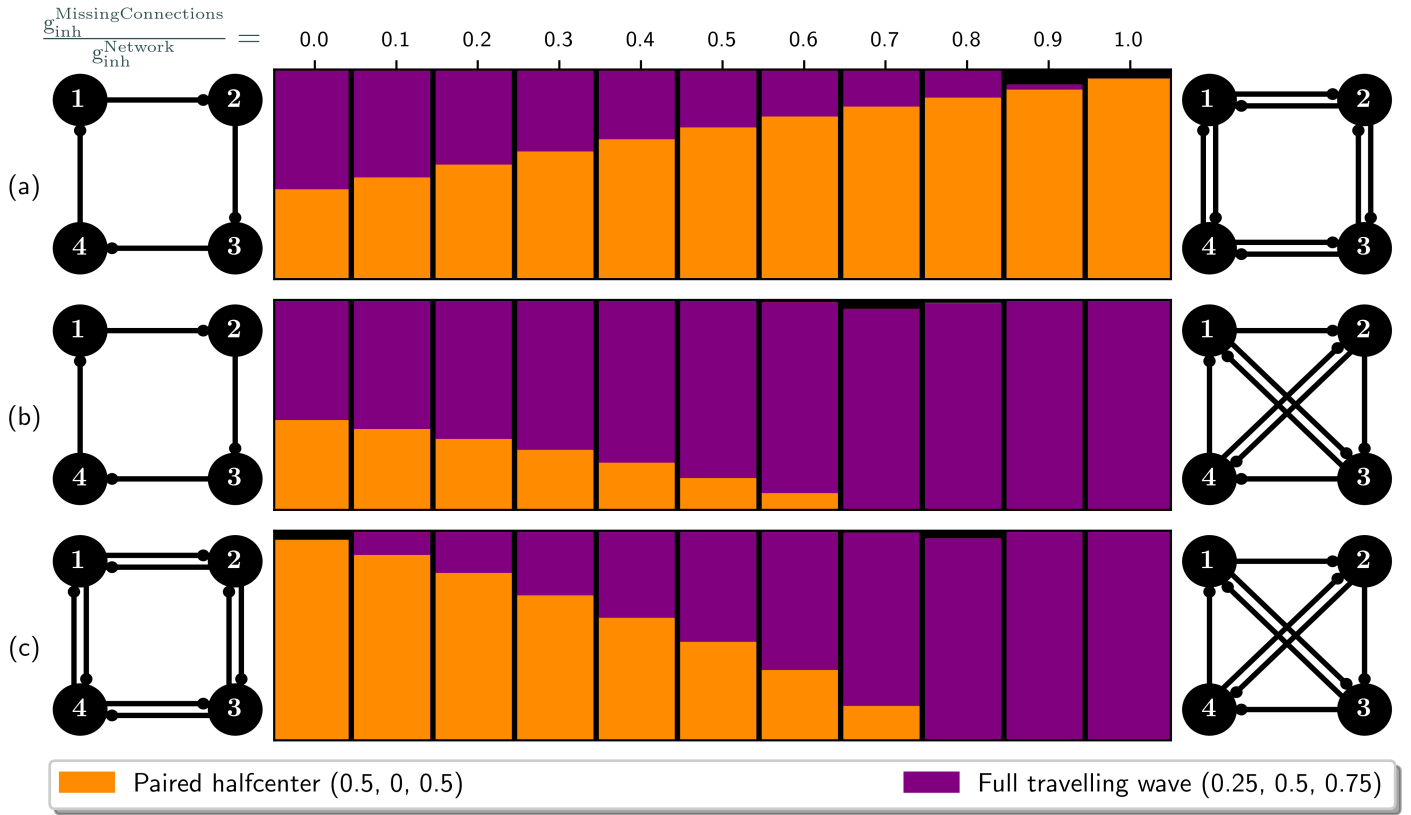
Figure 8: Structural changes in a network promote or suppress rhythmic behaviors. Gradual strengthening or weakening of the synapses converts the circuits on the left into the circuits on the right. Purple regions represent the 4-phasic full traveling-wave rhythm of $(0.25, 0.5, 0.75)$ while orange regions represent the 2-phasic paired half-center $(0.5, 0., 0.5)$, with sizes proportional to their attractors in the phase space. One-way inhibitory loop network exhibits robust bistability with both these rhythms while two-way inhibitory loop and mixed networks show robust mono-stability with the paired half-center and the traveling-wave pattern, respectively. (a) Transition from bistability to monostable paired half-center rhythm while the traveling-wave rhythm is gradually suppressed. (b) Bistable network transitions to monostable traveling-wave rhythm. (c) Transitions from one monostable rhythm (paired half-center) to another (full traveling-wave). At intermediate synaptic changes when not all synapses between the neurons have equal strengths, the network is bistable. Here, $g_{inh}^{Network} = 0.029$, $I_{app} = 0.54$ and $\varepsilon = 0.3$

4. Conclusions and future directions

In summary, we combine the existing techniques of dynamical systems theory with modern computational approaches such as unsupervised machine learning (clustering) algorithms and faster GPU-parallelized simulations of heavily populated trajectories to reveal the rhythmic capacities of homogenous 4-cell networks. This study extends our knowledge of the basic principles guiding multi-stable rhythmic behaviors in such neural networks and allows us to predict the changes in patterns of activity and multistability, based on changes in the network configurations and external inputs. We demonstrate how inhibitory coupled 4-cell networks can exhibit a plethora of monostable or multistable rhythmic states composed of pacemakers, paired half-centers, full and mixed traveling-waves, synchronized states, and chimeras. We identify the transitions and bifurcations that occur with changing network topologies, intrinsic cellular properties, synaptic and external drives to identify factors promoting or suppressing monostable/multistable rhythmic output. This can generate verifiable hypotheses for neurophysiological experiments and manipulations of real animal CPGs with dynamic clamp technique. We identify network topologies that produce robust monostable rhythms and are resilient to external perturbations.

Our analysis can help non-biological systems from engineering, economics, and environmental studies, where loss of resilience is a challenge to predict and can cause catastrophic effects. Such understanding is also essential to study motor control, dynamic memory, information processing, and decision making in animals and humans [65]. It also has implications for gaining insights into complex neurological phenomena in higher animals along with neurological disorders related to CPG arrhythmia, and the development of mechanisms to treat such disorders. Before such techniques can be applied to humans, we need to achieve a comprehensive understanding of the working of these modular networks in lower animals and through computational models. While this project deals with networks of single neurons, the methodology might also be applied to study networks of brain regions or neural populations that synergistically excite or inhibit each other and produce rhythmic patterns of firing [66, 67]. The insights in CPG multistability gained from this research might help in the design and development of more efficient robot locomotion [68, 69, 70, 71, 72, 73, 74, 75, 76, 77, 78, 79]. An important aspect of these analytical and computational techniques is their validity across a wide range of oscillatory networks without

dependence on the underlying mathematical equations. Hence they are applicable to a variety of rhythmic neuronal and non-neuronal activities beyond motor control and will benefit a wide audience of interdisciplinary researchers for studies of diverse nonlinear applications.

Acknowledgements

References

[1] E. Bullmore, O. Sporns, Complex brain networks: graph theoretical analysis of structural and functional systems, Nature Reviews Neuroscience 10 (3) (2009) 186.

[2] F. Azam, Biologically inspired modular neural networks, Ph.D. thesis, Virginia Tech (2000).

[3] D. Meunier, R. Lambiotte, E. T. Bullmore, Modular and hierarchically modular organization of brain networks, Frontiers in neuroscience 4 (2010) 200.

[4] O. Sporns, R. Kötter, Motifs in brain networks, PLoS biology 2 (11) (2004) e369.

[5] J. P. Miller, A. I. Selverston, Neural mechanisms for the production of the lobster pyloric motor pattern, in: Model neural networks and behavior, Springer, 1985, pp. 37–48.

[6] T. Bal, F. Nagy, M. Moulins, The pyloric central pattern generator in crustacea: a set of conditional neuronal oscillators, Journal of Comparative Physiology A 163 (6) (1988) 715–727.

[7] E. Marder, R. L. Calabrese, Principles of rhythmic motor pattern generation, Physiological reviews 76 (3) (1996) 687–717.

[8] W. B. Kristan Jr, R. L. Calabrese, W. O. Friesen, Neuronal control of leech behavior, Progress in neurobiology 76 (5) (2005) 279–327.

[9] R. J. Calin-Jageman, M. J. Tunstall, B. D. Mensh, P. S. Katz, W. N. Frost, Parameter space analysis suggests multi-site plasticity contributes to motor pattern initiation in tritonia, Journal of Neurophysiology 98 (4) (2007) 2382–2398.

[10] W. E. Sherwood, R. Harris-Warrick, J. Guckenheimer, Synaptic patterning of left-right alternation in a computational model of the rodent hindlimb central pattern generator, Journal of computational neuroscience 30 (2) (2011) 323–360.

[11] J. M. Newcomb, A. Sakurai, J. L. Lillvis, C. A. Gunaratne, P. S. Katz, Homology and homoplasy of swimming behaviors and neural circuits in the nudipleura (mollusca, gastropoda, opisthobranchia), Proceedings of the National Academy of Sciences 109 (Supplement 1) (2012) 10669–10676.

[12] R. Milo, S. Shen-Orr, S. Itzkovitz, N. Kashtan, D. Chklovskii, U. Alon, Network motifs: simple building blocks of complex networks, Science 298 (5594) (2002) 824–827.

[13] M. I. Rabinovich, P. Varona, A. I. Selverston, H. D. Abarbanel, Dynamical principles in neuroscience, Reviews of modern physics 78 (4) (2006) 1213.

[14] A. Bulloch, N. Syed, Reconstruction of neuronal networks in culture, Trends in Neurosciences 15 (11) (1992) 422–427.

[15] E. Marder, Invertebrate neurobiology: Polymorphic neural networks, Current Biology 4 (8) (1994) 752–754.

[16] W. N. Frost, P. S. Katz, Single neuron control over a complex motor program, Proceedings of the National Academy of Sciences 93 (1) (1996) 422–426.

[17] P. S. Katz, Evolution of central pattern generators and rhythmic behaviours, Philosophical Transactions of the Royal Society B 371 (1685) (2016) 20150057–20150057.

[18] J. Wojcik, J. Schwabedal, R. Clewley, A. L. Shilnikov, Key bifurcations of bursting polyrhythms in 3-cell central pattern generators, PloS one 9 (4) (2014) e92918.

[19] D. Alacam, A. Shilnikov, Making a swim central pattern generator out of latent parabolic bursters, International Journal of Bifurcation and Chaos 25 (07) (2015) 1540003.

[20] J. Wojcik, R. Clewley, A. Shilnikov, Order parameter for bursting polyrhythms in multifunctional central pattern generators, Physical Review E 83 (5) (2011) 056209.

[21] T. G. Brown, The intrinsic factors in the act of progression in the mammal, Proc. R. Soc. Lond. B 84 (572) (1911) 308–319.

[22] S. Jalil, D. Allen, J. Youker, A. Shilnikov, Toward robust phase-locking in melibe swim central pattern generator models, Chaos: An Interdisciplinary Journal of Nonlinear Science 23 (4) (2013) 046105.

[23] A. Sakurai, P. Katz, Distinct neural circuit architectures produce analogous rhythmic behaviors in related species, in: Soc. Neurosci. Abstr, Vol. 37, 2011.

[24] A. Sakurai, J. M. Newcomb, J. L. Lillvis, P. S. Katz, Different roles for homologous interneurons in species exhibiting similar rhythmic behaviors, Current Biology 21 (12) (2011) 1036–1043.

[25] A. Sakurai, C. A. Gunaratne, P. S. Katz, Two interconnected kernels of reciprocally inhibitory interneurons underlie alternating left-right swim motor pattern generation in the mollusk melibe leonina, Journal of neurophysiology 112 (6) (2014) 1317–1328.

[26] P. S. Katz, Comparison of extrinsic and intrinsic neuromodulation in two central pattern generator circuits in invertebrates, Experimental Physiology 83 (3) (1998) 281–292.

[27] N. Kopell, B. Ermentrout, Chemical and electrical synapses perform complementary roles in the synchronization of interneuronal networks, Proceedings of the National Academy of Sciences 101 (43) (2004) 15482–15487.

[28] K. Matsuoka, Mechanisms of frequency and pattern control in the neural rhythm generators, Biological cybernetics 56 (5-6) (1987) 345–353.

[29] N. Kopell, Toward a theory of modelling generators, Neural control of rhythmic movements in vertebrates.

[30] C. Canavier, D. Baxter, J. Clark, J. Byrne, Multiple modes of activity in a model neuron suggest a novel mechanism for the effects of neuromodulators, Journal of neurophysiology 72 (2) (1994) 872–882.

[31] F. Skinner, N. Kopell, E. Marder, Mechanisms for oscillation and frequency control in networks of mutually inhibitory relaxation oscillators, J. Comput. Neurosci 1 (1994) 69–87.

[32] R. Dror, C. C. Canavier, R. J. Butera, J. W. Clark, J. H. Byrne, A mathematical criterion based on phase response curves for stability in a ring of coupled oscillators, Biological cybernetics 80 (1) (1999) 11–23.

[33] A. A. Prinz, C. P. Billimoria, E. Marder, Alternative to hand-tuning conductance-based models: construction and analysis of databases of model neurons, Journal of neurophysiology 90 (6) (2003) 3998–4015.

[34] J. E. Rubin, D. Terman, Explicit maps to predict activation order in multiphase rhythms of a coupled cell network, The Journal of Mathematical Neuroscience 2 (1) (2012) 4.

[35] W. B. Kristan, Neuronal decision-making circuits, Current Biology 18 (19) (2008) R928–R932.

[36] K. L. Briggman, W. Kristan Jr, Multifunctional pattern-generating circuits, Annu. Rev. Neurosci. 31 (2008) 271–294.

[37] J. Collens, Rhythmogenesis and bifurcation analysis of 3-node neural network kernels.

[38] T. Xing, Computational study in chaotic dynamical systems and mechanisms for pattern generation in three-cell networks.

[39] D. Alacam, Modeling rhythm generation in swim central pattern generator of melibe leonina.

[40] A. Sakurai, P. S. Katz, Artificial synaptic rewiring demonstrates that distinct neural circuit configurations underlie homologous behaviors, Current Biology 27 (12) (2017) 1721–1734.

[41] A. Shilnikov, R. Gordon, I. Belykh, Polyrhythmic synchronization in bursting networking motifs, Chaos: An Interdisciplinary Journal of Nonlinear Science 18 (3) (2008) 037120.

[42] R. L. Calabrese, B. J. Norris, A. Wenning, T. M. Wright, Coping with variability in small neuronal networks (2011).

[43] J. T. Schwabedal, D. E. Knapper, A. L. Shilnikov, Qualitative and quantitative stability analysis of penta-rhythmic circuits, Nonlinearity 29 (12) (2016) 3647.

[44] A. Shilnikov, Complete dynamical analysis of a neuron model, Nonlinear Dynamics 68 (3) (2012) 305–328.

[45] J. Rubin, D. Terman, Geometric analysis of population rhythms in synaptically coupled neuronal networks, Neural computation 12 (3) (2000) 597–645.

[46] F. Skinner, L. Zhang, J. P. Velazquez, P. Carlen, Bursting in inhibitory interneuronal networks: a role for gap-junctional coupling, Journal of neurophysiology 81 (3) (1999) 1274–1283.

[47] C. Van Vreeswijk, L. Abbott, G. B. Ermentrout, When inhibition not excitation synchronizes neural firing, Journal of computational neuroscience 1 (4) (1994) 313–321.

[48] S. Jalil, I. Belykh, A. Shilnikov, Fast reciprocal inhibition can synchronize bursting neurons, Physical Review E 81 (4) (2010) 045201.

[49] S. Jalil, I. Belykh, A. Shilnikov, Spikes matter in phase-locking of inhibitory bursting networks, Phys Rev E 85 (2012) 36214.

[50] W. Wang, L. Xu, J. Cavazos, H. H. Huang, M. Kay, Fast acceleration of 2d wave propagation simulations using modern computational accelerators, PloS one 9 (1) (2014) e86484.

[51] K. Pusuluri, A. Shilnikov, Homoclinic chaos and its organization in a nonlinear optics model, Phys. Rev. E 98 (2018) 040202. doi:10.1103/PhysRevE.98.040202.
URL https://link.aps.org/doi/10.1103/PhysRevE.98.040202

[52] K. Pusuluri, A. Pikovsky, A. Shilnikov, Unraveling the chaos-land and its organization in the rabinovich system, in: Advances in Dynamics, Patterns, Cognition, Springer, 2017, pp. 41–60.

[53] K. Pusuluri, A. Shilnikov, Symbolic representation of neuronal dynamics (in print), in: Advances on Nonlinear Dynamics of Electronic Systems, Springer, 2017, Ch. 17.

[54] E. Yavuz, J. Turner, T. Nowotny, Genn: a code generation framework for accelerated brain simulations, Scientific reports 6 (2016) 18854.

[55] D. S. Wilks, Cluster analysis, in: International geophysics, Vol. 100, Elsevier, 2011, pp. 603–616.

[56] A. K. Jain, M. N. Murty, P. J. Flynn, Data clustering: a review, ACM computing surveys (CSUR) 31 (3) (1999) 264–323.

[57] M. Längkvist, L. Karlsson, A. Loutfi, A review of unsupervised feature learning and deep learning for time-series modeling, Pattern Recognition Letters 42 (2014) 11–24.

[58] F. Pedregosa, G. Varoquaux, A. Gramfort, V. Michel, B. Thirion, O. Grisel, M. Blondel, P. Prettenhofer, R. Weiss, V. Dubourg, et al., Scikit-learn: Machine learning in python, Journal of machine learning research 12 (Oct) (2011) 2825–2830.

[59] F. Murtagh, A survey of recent advances in hierarchical clustering algorithms, The Computer Journal 26 (4) (1983) 354–359.

[60] R. Gentleman, V. Carey, Unsupervised machine learning, in: Bioconductor Case Studies, Springer, 2008, pp. 137–157.

[61] S. C. Johnson, Hierarchical clustering schemes, Psychometrika 32 (3) (1967) 241–254.

[62] N. W. Schultheiss, A. A. Prinz, R. J. Butera, Phase response curves in neuroscience: theory, experiment, and analysis, Springer Science & Business Media, 2011.

[63] I. Belykh, E. de Lange, M. Hasler, Synchronization of bursting neurons: What matters in the network topology, Physical review letters 94 (18) (2005) 188101.

[64] I. Kemenes, V. Marra, M. Crossley, D. Samu, K. Staras, G. Kemenes, T. Nowotny, Dynamic clamp with stdpc software, Nature protocols 6 (3) (2011) 405.

[65] T. Kee, P. Sanda, N. Gupta, M. Stopfer, M. Bazhenov, Feed-forward versus feedback inhibition in a basic olfactory circuit, PLoS computational biology 11 (10) (2015) e1004531.

[66] G. Deco, G. Tononi, M. Boly, M. L. Kringelbach, Rethinking segregation and integration: contributions of whole-brain modelling, Nature Reviews Neuroscience 16 (7) (2015) 430.

[67] V. K. Jirsa, W. C. Stacey, P. P. Quilichini, A. I. Ivanov, C. Bernard, On the nature of seizure dynamics, Brain 137 (8) (2014) 2210–2230.

[68] G. Ren, W. Chen, S. Dasgupta, C. Kolodziejski, F. Wörgötter, P. Manoonpong, Multiple chaotic central pattern generators with learning for legged locomotion and malfunction compensation, Information Sciences 294 (2015) 666–682.

[69] P. Kaluza, T. Cioacă, Phase oscillator neural network as artificial central pattern generator for robots, Neurocomputing 97 (2012) 115–124.

[70] A. J. Ijspeert, Central pattern generators for locomotion control in animals and robots: a review, Neural networks 21 (4) (2008) 642–653.

[71] J. H. Barron-Zambrano, C. Torres-Huitzil, Cpg implementations for robot locomotion: Analysis and design, in: Robotic Systems-Applications, Control and Programming, InTech, 2012.

[72] T. Mori, Y. Nakamura, M.-A. Sato, S. Ishii, Reinforcement learning for cpg-driven biped robot, in: AAAI, Vol. 4, 2004, pp. 623–630.

[73] A. Nogaret, E. L. O'callaghan, R. M. Lataro, H. C. Salgado, C. D. Meliza, E. Duncan, H. D. Abarbanel, J. F. Paton, Silicon central pattern generators for cardiac diseases, The Journal of physiology 593 (4) (2015) 763–774.

[74] P. Eckert, A. Spröwitz, H. Witte, A. J. Ijspeert, Comparing the effect of different spine and leg designs for a small bounding quadruped robot, in: Robotics and Automation (ICRA), 2015 IEEE International Conference on, IEEE, 2015, pp. 3128–3133.

[75] A. T. Sprowitz, A. Tuleu, A. J. Ijspeert, et al., Kinematic primitives for walking and trotting gaits of a quadruped robot with compliant legs, Frontiers in computational neuroscience 8 (2014) 27.

[76] L. Righetti, A. J. Ijspeert, Pattern generators with sensory feedback for the control of quadruped locomotion, in: Robotics and Automation, 2008. ICRA 2008. IEEE International Conference on, IEEE, 2008, pp. 819–824.

[77] A. J. Ijspeert, A. Crespi, D. Ryczko, J.-M. Cabelguen, From swimming to walking with a salamander robot driven by a spinal cord model, science 315 (5817) (2007) 1416–1420.

[78] A. J. Ijspeert, Biorobotics: Using robots to emulate and investigate agile locomotion, science 346 (6206) (2014) 196–203.

[79] N. S. Szczecinski, A. E. Brown, J. A. Bender, R. D. Quinn, R. E. Ritzmann, A neuromechanical simulation of insect walking and transition to turning of the cockroach blaberus discoidalis, Biological cybernetics 108 (1) (2014) 1–21.

Computational exposition of multistable dynamics in neural circuits
Supplementary Material

Krishna Pusuluri, Sunitha Basodi, and Andrey Shilnikov

(Dated: June 12, 2019)

470

Movie M1: Full travelling wave rhythm seen in the fully connected 4-cell circuit at $I_{app} = 0.505$, $g_{inh} = 0.025$ and $\varepsilon = 0.5$

Movie M2: Rhythm converging to a paired half-center in the fully connected 4-cell circuit at $I_{app} = 0.435$, $g_{inh} = 0.025$ and $\varepsilon = 0.5$ (Fig. 5B)

Movie M3: Rhythm converging to the synchronized state in the fully connected 4-cell circuit at $I_{app} = 0.435$, $g_{inh} = 0.025$

475 and $\varepsilon = 0.5$ (Fig. 5B)

Movie M4: Period doubling of the orbit for the synchronized state in the fully connected 4-cell circuit, resulting in phase synchronization of all the 4 neurons, but with pairs of cells alternating between orbits of smaller and larger amplitudes.
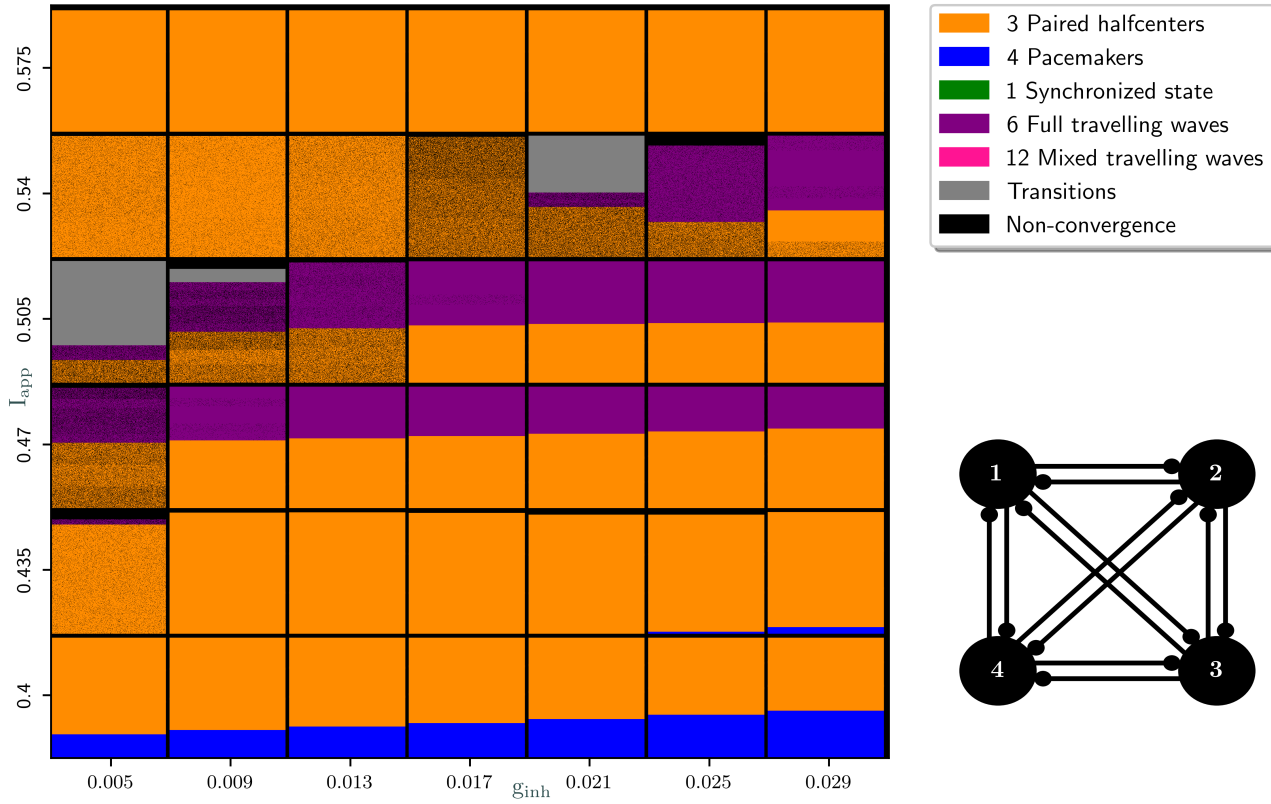

Figure S1: Multistability and bifurcation analysis of the fully connected 4-cell network at $\varepsilon = 0.3$ shows similar rhythmic capacity as Fig.5 (at $\varepsilon = 0.5$), except for the lack of stable synchronized state.
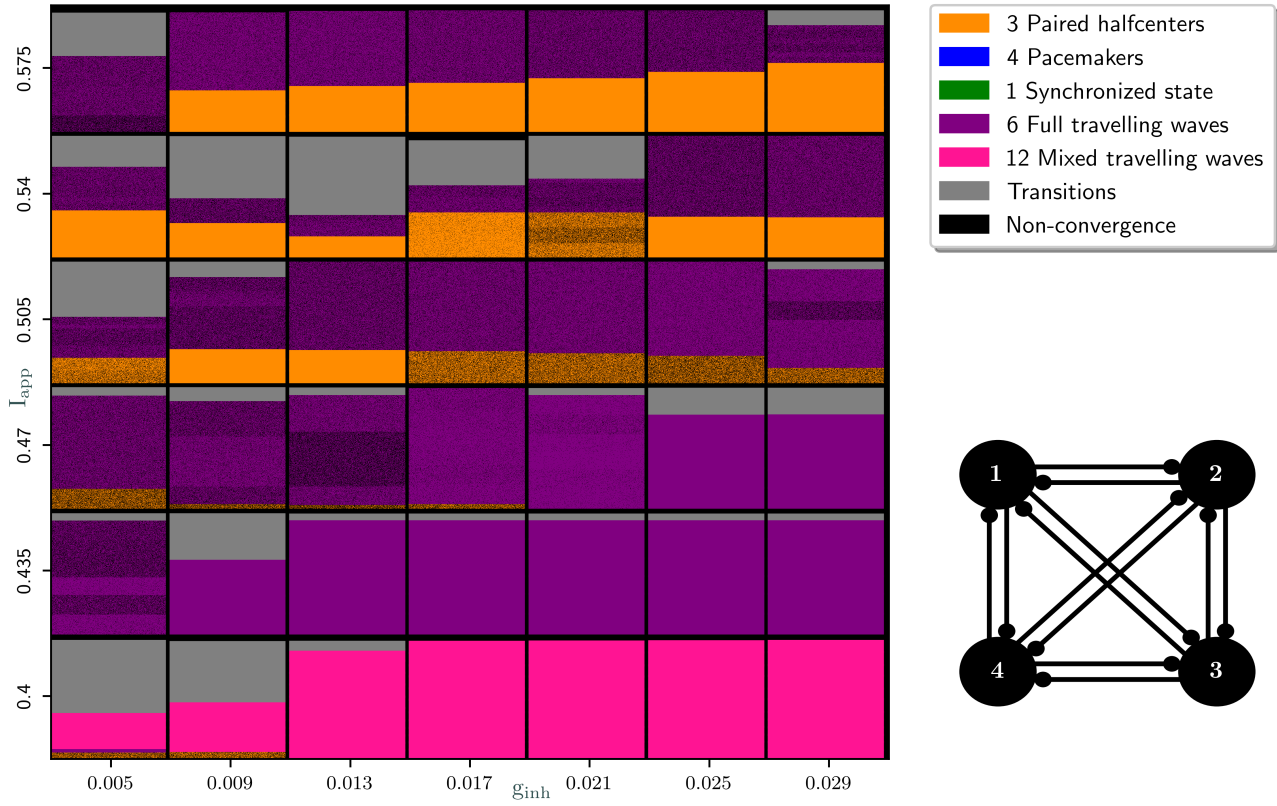
Figure S2: Multistability and bifurcation analysis of the fully connected 4-cell circuit at $\varepsilon = 0.05$ shows the dominant expression of the traveling-wave (full and mixed) rhythms, compared to the paired half-centers.
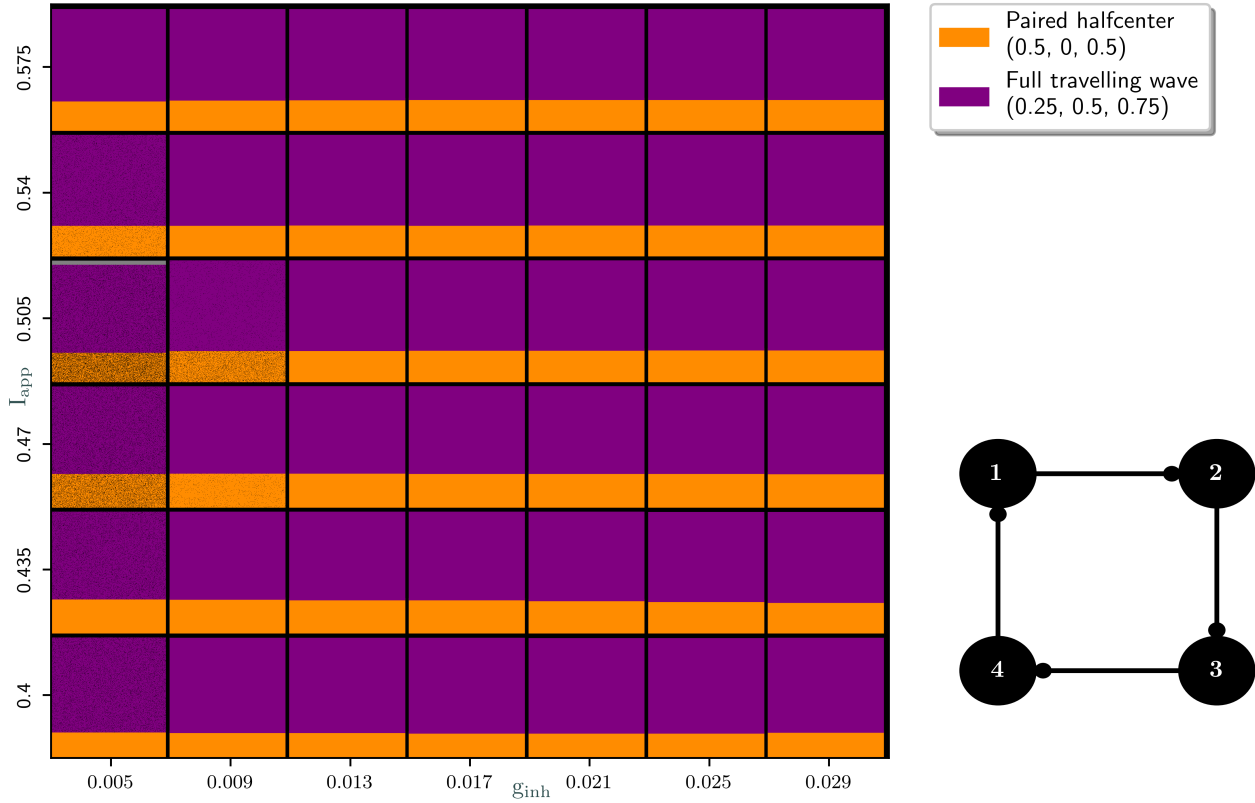

Figure S3: Robust bistability of the one-way inhibitory loop network with the full travelling wave rhythm of $(0.25, 0.5, 0.75)$ and the paired half-center $(0.5, 0., 0.5)$. No other stable isomorphisms of these rhythms exist due to the missing synaptic connections compared to the fully connected network. $\varepsilon = 0.5$.
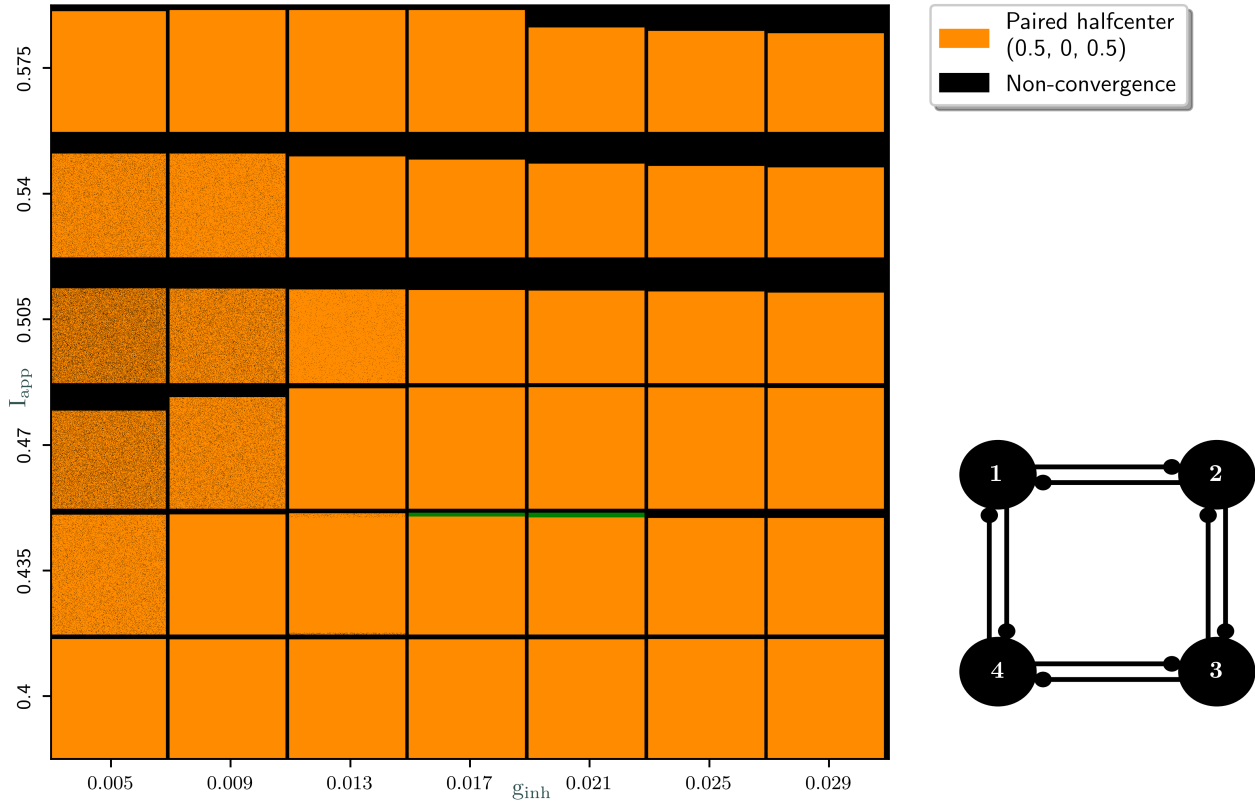
Figure S4: Robust monostability of the two-way inhibitory loop network with the paired half-center rhythm $(0.5, 0., 0.5)$ (no other stable isomorphisms). $\varepsilon = 0.5$.
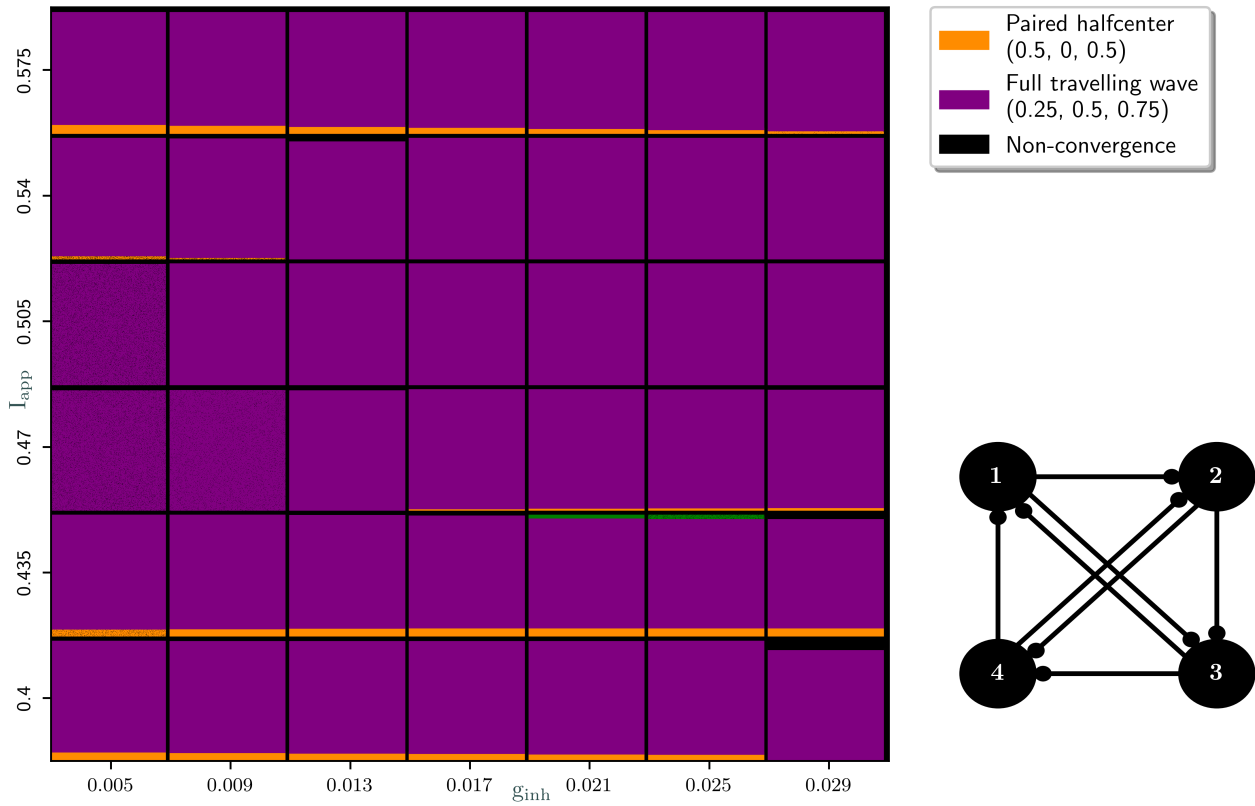

Figure S5: Robust monostability of the mixed network with the full travelling wave rhythm of $(0.25, 0.5, 0.75)$ (no other stable isomorphisms). $\varepsilon = 0.5$.